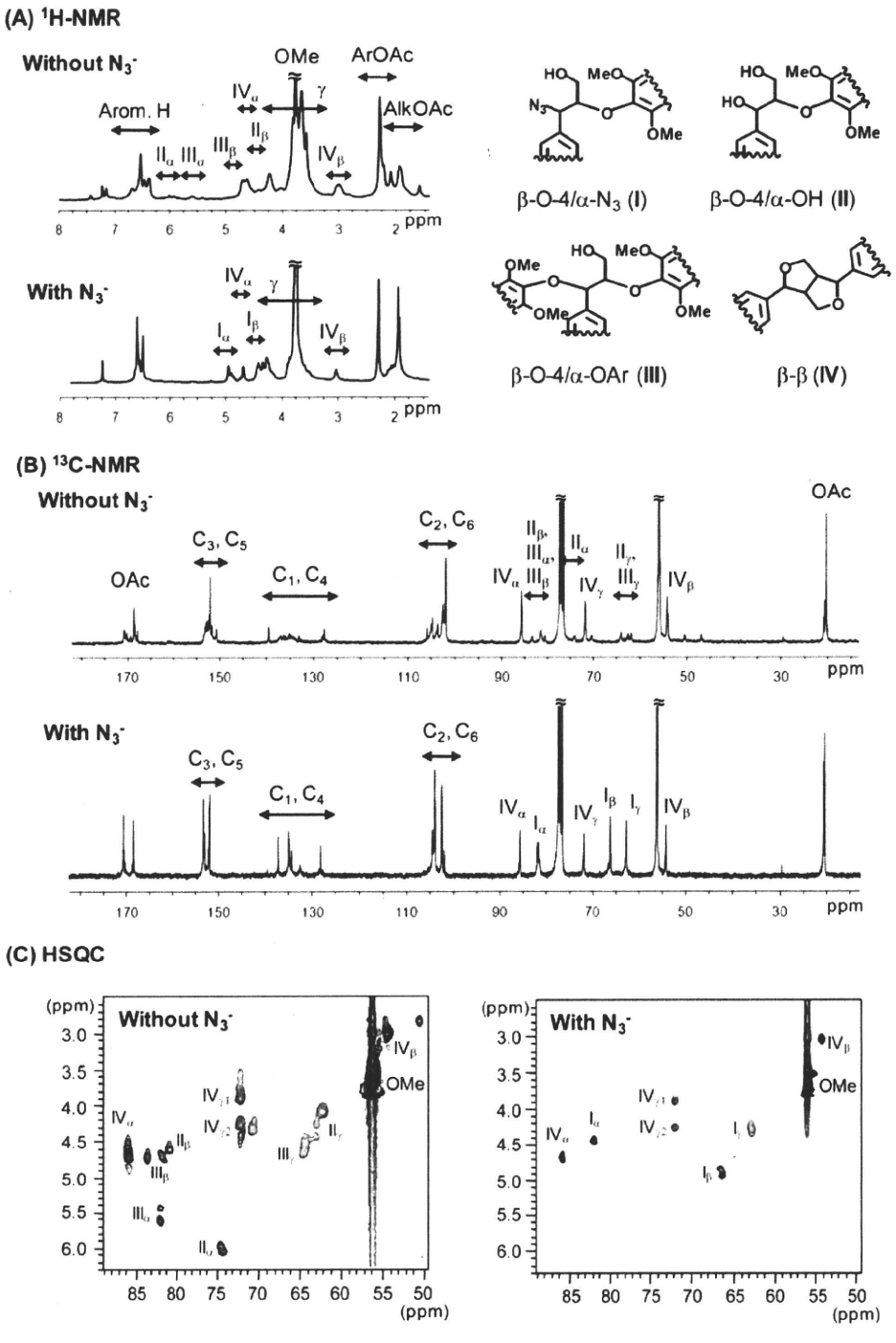

Fig. 7. Nuclear magnetic resonance (NMR) characterizations of acetylated S-DHPs from S-alc synthesized in the presence of azide ion. **A** ^{1}H-NMR spectra. **B** ^{13}C-NMR spectra. **C** 2D-heteronuclear single quantum coherence (HSQC) spectra

ion tend to have slightly lower molecular mass and narrower molecular mass distributions than those of conventional S-DHPs (see Table 1). This difference might be explained by the lack of structure **III** in the S-DHPs prepared with azide ion, as the branching structure **III** is formed by nucleophilic attacks of oligomeric phenolics onto *β-O-4* S-QM.

Conclusions

To examine the contribution of reactivity of S-QM on S-DHP production from S-alc, HRP-catalyzed dehydrogenative polymerization in the presence of nucleophilic reagents was investigated. The HRP-catalyzed polymerization of

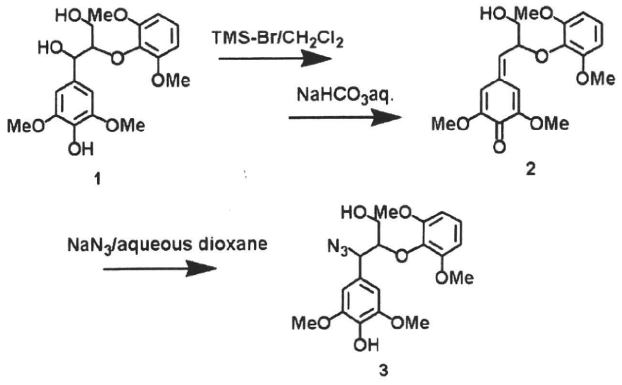

Fig. 8. Synthetic scheme for model compound **3**. TMS, trimethylsilyl

iso-S, which permits monitoring the formation of S-QM in a homogeneous aqueous phase, was successfully utilized for screening of a nucleophile used as a S-QM scavenger in the polymerization of S-alc. UV spectroscopic monitoring of iso-S polymerization in the presence of various nucleophiles revealed the high ability of azide ion to trap S-QM without significant inhibition of HRP activity. GPC-PDA monitoring of the polymerization of iso-S also demonstrated that the oligomeric S-QM efficiently converted to S-DHP in the presence of azide ion. Accordingly, azide ion was applied as a S-QM scavenger in HRP-catalyzed polymerization of S-alc, resulting in production of S-DHPs in remarkably high yields. Although azide ion dramatically promotes the production of S-DHP, the molecular mass of the isolated S-DHPs was not improved as much, which is partly explained by the lack of branching α-*O*-4 structures (**III**) in the S-DHPs prepared with azide ion. NMR analyses on S-DHPs clearly demonstrated that azide ion efficiently performed nucleophilic additions to the C-α of the S-QM during the polymerization. It was demonstrated that, in the HRP-catalyzed polymerization of S-alc in the presence of strongly nucleophilic azide ion, S-QM are readily rearomatized by azide addition. Then, subsequent polymerization steps, initiated by the oxidation of the regenerated phenolic hydroxyl groups, can proceed repeatedly to yield S-DHPs efficiently. Consequently, these data provide experimental proof that the low reactivity of S-QM with nucleophiles in the conventional polymerization system is a crucial cause of low efficiency in the dehydrogenative polymerization of S-alc in vitro. Because there seems to be no evidence that any particular nucleophilic reagents operate in lignin formation in vivo, subsequent studies should focus on the reactions of S-QM under various polymerization conditions without the use of strongly nucleophilic reagents. Such studies are expected to provide new clues for understanding the factors controlling lignin polymerization in the plant cell.

Acknowledgments This research was supported by a Grant-in-Aid for Young Scientists (#20-2841) from the Japan Society for the Promotion of Science (JSPS).

References

1. Freudenberg K (1965) Lignin. Its constitution and formation from *p*-hydroxycinnamyl alcohols. Science 148:595–600
2. Sarkanen KV (1971) Precursors and their polymerization. In: Sarkanen KV, Ludwig CH (eds) Lignins: occurrence, formation, structure and reactions. Wiley, New York, pp 95–163
3. Higuchi T (1990) Lignin biochemistry: biosynthesis and biodegradation. Wood Sci Technol 24:23–63
4. Boerjan W, Ralph J, Baucher M (2003) Lignin biosynthesis. Annu Rev Plant Biol 54:519–546
5. Ralph J, Lundquist K, Brunow G, Lu F, Kim H, Schatz PF, Marita JM, Hatfield RD, Ralph SA, Christensen JH, Boerjan W (2004) Lignins: natural polymers from oxidative coupling of 4-hydroxyphenylpropanoids. Phytochem Rev 3:29–60
6. Monties B (2005) Biological variability of lignins. Cell Chem Technol 39:341–367
7. Grabber JH (2005) How do lignin composition, structure, and cross-linking affect degradability? A review of cell wall model studies. Crop Sci 45:820–831
8. Ralph J, Brunow G, Harris PJ, Dixon RA, Schatz PF, Boerjan W (2008) Lignification: are lignins biosynthesized via simple combinatorial chemistry or via proteinaceous control and template replication? Recent Adv Polyphenol Res 1:36–66
9. Freudenberg K, Hübner HH (1952) Hydroxycinnamyl alcohols and their dehydrogenation polymers. Chem Ber 85:1181–1191
10. Yamasaki T, Hata K, Higuchi T (1976) Dehydrogenation polymer of sinapyl alcohol by peroxidase and hydrogen peroxide. Mokuzai Gakkaishi 22:582–588
11. Faix O, Besold G (1978) Preparation and characterization of dehydrogenation polymers of *p*-hydroxycinnamic alcohols (DHPs) particularly made from pure 4-hydroxyphenyl-(H-), guajacyl-(G-) and syringyl-(S-) propane polymers. I. Elemental analysis and determination of functional groups. Holzforschung 32:1–7
12. Weymouth N, Dean J FD, Eriksson KEL, Morrison WH III, Himmelsbach DS, Hartley RD (1993) Synthesis and spectroscopic characterization of *p*-hydroxyphenyl, guaiacyl and syringyl lignin polymer models (DHPs). Nord Pulp Pap Res J 8:344–349
13. Sterjiades R, Dean JFD, Gamble G, Himmelsbach DS, Eriksson KEL (1993) Extracellular laccases and peroxidases from sycamore maple (*Acer pseudoplatanus*) cell-suspension cultures. Reactions with monolignols and lignin model compounds. Planta (Berl) 190:75–87
14. Yoshida S, Chatani A, Tanahashi M, Honda Y, Watanabe T, Kuwahara M (1998) Preparation of synthetic lignin by manganese peroxidase of *Bjerkandera adusta* in organic solvents. Holzforschung 52:282–286
15. Tobimatsu Y, Takano T, Kamitakahara H, Nakatsubo F (2008) Studies on the dehydrogenative polymerizations of monolignol β-glycosides. Part 3: Horseradish peroxidase-catalyzed polymerizations of triandrin and isosyringin. J Wood Chem Technol 28: 69–83
16. Ostergaard L, Teilum K, Mirza O, Mattsson O, Petersen M, Welinder KG, Mundy J, Gajhede M, Henriksen A (2000) *Arabidopsis* ATP A2 peroxidase. Expression and high-resolution structure of a plant peroxidase with implications for lignification. Plant Mol Biol 44:231–243
17. Nielsen KL, Indiani C, Henriksen A, Feis A, Becucci M, Gajhede M, Smulevich G, Welinder KG (2001) Differential activity and structure of highly similar peroxidases. Spectroscopic, crystallographic, and enzymatic analyses of lignifying *Arabidopsis thaliana* peroxidase A2 and horseradish peroxidase A2. Biochemistry 40:11013–11021
18. Aoyama W, Sasaki S, Matsumura S, Mitsunaga T, Hirai H, Tsutsumi Y, Nishida T (2002) Sinapyl alcohol-specific peroxidase isoenzyme catalyzes the formation of the dehydrogenative polymer from sinapyl alcohol. J Wood Sci 48:497–504
19. Sasaki S, Nishida T, Tsutsumi Y, Kondo R (2004) Lignin dehydrogenative polymerization mechanism: a poplar cell wall peroxidase directly oxidizes polymer lignin and produces in vitro dehydrogenative polymer rich in β-O-4 linkage. FEBS Lett 562:197–201
20. Kobayashi T, Taguchi H, Shigematsu M, Tanahashi M (2005) Substituent effects of 3,5-disubstituted *p*-coumaryl alcohols on their

oxidation using horseradish peroxidase-H_2O_2 as the oxidant. J Wood Sci 51:607–614
21. Tanahashi M, Takeuchi H, Higuchi T (1976) Dehydrogenative polymerization of 3,5-substituted *p*-coumaryl alcohols. Wood Res 61:44–53
22. Tanahashi M, Higuchi T (1990) Effect of the hydrophobic regions of hemicelluloses on dehydrogenative polymerization of sinapyl alcohol. Mokuzai Gakkaishi 36:424–428
23. Takano T, Tobimatsu Y, Hosoya T, Hattori T, Ohnishi J, Takano M, Kamitakahara H, Nakatsubo F (2006) Studies on the dehydrogenative polymerizations of monolignol β-glycosides. Part 1. Syntheses of monolignol β-glycosides, (*E*)-isoconiferin, (*E*)-isosyringin, and (*E*)-triandrin. J Wood Chem Technol 26:215–229
24. Tobimatsu Y, Takano T, Kamitakahara H, Nakatsubo F (2006) Studies on the dehydrogenative polymerizations of monolignol β-glycosides. Part 2: Horseradish peroxidase-catalyzed dehydrogenative polymerization of isoconiferin. Holzforschung 60:513–518
25. Tobimatsu Y, Takano T, Kamitakahara H, Nakatsubo F (2008) Studies on the dehydrogenative polymerizations (DHPs) of monolignol β-glycosides: part 4. Horseradish peroxidase-catalyzed copolymerization of isoconiferin and isosyringin. Holzforschung 62: 495–500
26. Tobimatsu Y, Takano T, Kamitakahara H, Nakatsubo F (2008) Studies on the dehydrogenative polymerization of monolignol β-glycosides: part 5. UV spectroscopic monitoring of horseradish peroxidase-catalyzed polymerization of monolignol glycosides. Holzforschung 62:501–507
27. Tobimatsu Y, Takano T, Kamitakahara H, Nakatsubo F (2010) Studies on the dehydrogenative polymerizations of monolignol β-glycosides. Part 6. Monitoring of horseradish peroxidase-catalyzed polymeriation of monolignol glycosides by GPC-PDA. Holzforschung (in press)
28. Bolton JL, Sevestre H, Ibe BO, Thompson JA (1990) Formation and reactivity of alternative quinone methides from butylated hydroxytoluene: possible explanation for species-specific pneumotoxicity. Chem Res Toxicol 3:65–70
29. Bolton JL, Valerio LGJ, Thompson JA (1992) The enzymic formation and chemical reactivity of quinone methides correlate with alkylphenol-induced toxicity in rat hepatocytes. Chem Res Toxicol 5:816–822
30. Tobimatsu Y, Takano T, Kamitakahara H, Nakatsubo F (2008) Azide ion as a quinone methide scavenger in the horseradish peroxidase-catalyzed polymerization of sinapyl alcohol. J Wood Sci 54:87–89
31. Quideau S, Ralph J (1992) Facile large-scale synthesis of coniferyl, sinapyl, and *p*-coumaryl alcohol. J Agric Food Chem 40:1108–1110
32. Nakatsubo F, Sato K, Higuchi T (1975) Synthesis of guaiacylglycerol-β-guaiacyl ether. Holzforschung 29:165–168
33. Sipilä J, Syrjanen K (1995) Synthesis and ^{13}C NMR spectroscopic characterization of six dimeric arylglycerol-β-aryl ether model compounds representative of syringyl and *p*-hydroxyphenyl structures in lignins. On the aldol reaction in β-ether preparation. Holzforschung 49:325–331
34. Ralph J, Young RA (1983) Stereochemical aspects of addition reactions involving lignin model quinone methides. J Wood Chem Technol 3:161–181
35. Brunow G, Sipilä J, Makela T (1989) On the mechanism of formation of noncyclic benzyl ethers during lignin biosynthesis. Part 1. The reactivity of β-*O*-4-quinone methides with phenols and alcohols. Holzforschung 43:55–59
36. Hauteville M, Lundquist K, VonUnge S (1986) NMR studies of lignins. 7. Proton NMR spectroscopic investigation of the distribution of *erythro* and *threo* forms of β-*O*-4 structures in lignins. Acta Chem Scand B 40:31–35
37. Toikka M, Sipilä J, Teleman A, Brunow G (1998) Lignin-carbohydrate model compounds. Formation of lignin-methyl arabinoside and lignin-methyl galactoside benzyl ethers via quinone methide intermediates. J Chem Soc Perkin Trans 1:3813–3818
38. Ramakrishnan K, Fisher J (1983) Nucleophilic trapping of 7,11-dideoxyanthracyclinone quinone methides. J Am Chem Soc 105: 7187–7188
39. Fisher J, Abdella BR, McLane KE (1985) Anthracycline antibiotic reduction by spinach ferredoxin-NADP+ reductase and ferredoxin. Biochemistry 24:3562–3571
40. Awad HM, Boersma MG, Vervoort J, Rietjens IMCM (2000) Peroxidase-catalyzed formation of quercetin quinone methide-glutathione adducts. Arch Biochem Biophys 378:224–233
41. Al Kazwini AT, O'Neill P, Cundall RB, Adams GE, Junino A, Maignan J (1992) Direct observation of the reaction of the quinonemethide from 5,6-dihydroxyindole with the nucleophilic azide ion. Tetrahedron Lett 33:3045–3048
42. Novak M, Kayser KJ, Brooks ME (1998) Azide and solvent trapping of electrophilic intermediates generated during the hydrolysis of *N*-(sulfonatooxy)-*N*-acetyl-4-aminostilbene. J Org Chem 63: 5489–5496
43. Richard JP, Toteva MM, Crugeiras J (2000) Structure-reactivity relationships and intrinsic reaction barriers for nucleophile additions to a quinone methide: a strongly resonance-stabilized carbocation. J Am Chem Soc 122:1664–1674
44. Veitch NC (2004) Horseradish peroxidase: a modern view of a classic enzyme. Phytochemistry 65:249–259
45. DeRycker J, Halliwell B (1978) Oxidation of thiol compounds by catalase and peroxidase in the presence of manganese (II) and phenols. Biochem Soc Trans 6:1343–1345
46. Burner U, Obinger C (1997) Transient-state and steady-state kinetics of the oxidation of aliphatic and aromatic thiols by horseradish peroxidase. FEBS Lett. 411:269–274
47. Faix O, Lange W, Besold G (1981) Molecular weight determinations of DHP'S from mixtures of precursors by steric exclusion chromatography (HPLC). Holzforschung 35:137–140
48. Cathala B, Saake B, Faix O, Monties B (1998) Evaluation of the reproducibility of the synthesis of dehydrogenation polymer models of lignin. Polym Degrad Stab 59:65–69

Original Research Article

Dementia and Geriatric Cognitive Disorders

Dement Geriatr Cogn Disord 2010;30:101–111
DOI: 10.1159/000318754

Accepted: June 15, 2010
Published online: August 21, 2010

Voxel-Based Analysis of Amyloid Positron Emission Tomography Probe [^{11}C]BF-227 Uptake in Mild Cognitive Impairment and Alzheimer's Disease

He Shao[a] Nobuyuki Okamura[a] Kentaro Sugi[a] Shozo Furumoto[a, b] Katsutoshi Furukawa[d] Manabu Tashiro[c] Ren Iwata[b] Hiroshi Matsuda[g] Yukitsuka Kudo[f] Hiroyuki Arai[d] Hiroshi Fukuda[e] Kazuhiko Yanai[a]

[a]Department of Pharmacology, Tohoku University Graduate School of Medicine, and Divisions of [b]Radiopharmaceutical Chemistry and [c]Cyclotron Nuclear Medicine, Cyclotron and Radioisotope Center, Tohoku University, and Departments of [d]Geriatrics and Gerontology, Division of Brain Sciences, and [e]Nuclear Medicine and Radiology, Institute of Development, Ageing and Cancer, Tohoku University, and [f]Innovation of New Biomedical Engineering Center, Tohoku University, Sendai, and [g]Department of Nuclear Medicine, Saitama Medical University, International Medical Center, Saitama, Japan

Key Words
Alzheimer's disease · Mild cognitive impairment · Positron emission tomography · Amyloid

Abstract
Aim: To determine early brain changes in the distribution of an amyloid positron emission tomography (PET) probe, ^{11}C-labeled BF-227 or [^{11}C]BF-227, in order to accurately predict the progression of mild cognitive impairment (MCI) to Alzheimer's disease (AD). ***Patients and Methods:*** Amyloid plaque burden was evaluated using [^{11}C]BF-227 PET in AD, MCI and aged normal controls. A voxel-based analysis of [^{11}C]BF-227 PET images was performed to characterize the culprit brain lesion in patients with MCI who were destined to progress to AD, referred to as MCI converters (MCI-C). In addition, binding characteristics of BF-227 to amyloid deposits were examined using postmortem AD brain samples. ***Results:*** Voxel-based statistical analyses of the BF-227 PET images clearly demonstrated an abnormal distribution of BF-227 mainly in the posterior association area in MCI-C and patients with AD. BF-227 uptake in the lateral temporal cortex was consistently observed in almost all MCI-C and patients with AD, and it distinguished MCI-C from MCI nonconverters. BF-227 binding strongly correlated with dense amyloid-β protein plaque density, but not with diffuse plaque density in the frontal cortex. ***Conclusion:*** BF-227 uptake in the lateral temporal cortex is a reliable indicator that can be used for predicting prognosis in patients with MCI.

Introduction

Alzheimer's disease (AD) is considered as the most common cause of dementia in the elderly. Since the extensive deposition of extracellular senile plaques is one of the pathological hallmarks of AD, many researchers have examined these lesions to try and understand the pathogenesis of AD. In 1984, amyloid-β protein (Aβ) was iso-

KARGER
Fax +41 61 306 12 34
E-Mail karger@karger.ch
www.karger.com

1420–8008/10/0302–0101$26.00/0

Accessible online at:
www.karger.com/dem

Nobuyuki Okamura, MD, PhD
Department of Pharmacology, Tohoku University School of Medicine
2-1 Seiryo-machi, Aoba-ku
Sendai 980-8575 (Japan)
Tel. +81 22 717 8058, Fax +81 22 717 8060, E-Mail oka@mail.tains.tohoku.ac.jp

lated from cerebrovascular amyloidosis [1], and in the following year, it was isolated from amyloid plaques and neurofibrillary tangles [2, 3]. Senile plaques, which are mostly composed of Aβ, are believed to accumulate years before the onset of cognitive decline in AD [4]. Ten years ago, the concept of amnestic mild cognitive impairment (MCI) was introduced by the Mayo Clinic group. Amnestic MCI is now considered to be an intermediate predementia stage in patients with AD. Approximately 10–15% of patients with MCI develop AD [5, 6].

Positron emission tomography (PET) imaging using an amyloid-binding agent is a valid method for in vivo evaluation of Aβ plaque burden [7]. Several small molecular amyloid-binding agents have been designed for monitoring amyloid deposits in patients with MCI and AD and for evaluating the efficacy of antiamyloid therapy [8–12]. Furthermore, we have developed several benzoxazole derivatives as potential candidates for amyloid PET probes [13, 14]. A PET study using ^{11}C-labeled BF-227, or [^{11}C]BF-227, successfully detected amyloid plaques in living patients with AD [10]. Recent clinical studies have demonstrated neocortical [^{11}C]BF-227 uptake in patients with MCI [11, 15]. This finding suggests that neocortical [^{11}C]BF-227 uptake could be a potential biomarker for predicting progression from MCI to AD. In previous studies, analysis of PET images was mainly based on analysis of regions of interest (ROI). To eliminate any prior hypothesis about ROI selection, we performed voxel-based analyses of whole brain regions and made comparisons between MCI, AD and aged normal control groups. After [^{11}C]BF-227 PET scanning, we prospectively followed patients with MCI and investigated the relationship between initial BF-227 uptake and prognosis from MCI. The purpose of this study was to explore early changes in the process of amyloid plaque deposition in AD and understand the pattern of neocortical BF-227 distribution for accurate prediction of prognosis in the MCI stage.

Patients and Methods

Subjects and Patients

[^{11}C]BF-227 PET scans were performed on 12 aged normal controls, 19 probable patients with AD and 14 patients with MCI. The patients with AD were recruited via the Tohoku University Hospital Dementia Patients Registry, and the diagnosis was made according to the National Institute of Neurological and Communicative Diseases and Stroke/Alzheimer's Disease and Related Disorders Association criteria [16]. The patients with AD were divided into 2 groups according to their clinical severity: AD1 (Mini-Mental State Examination, MMSE, score ≥20) and AD2 (MMSE score <20). The diagnosis of amnestic MCI was made according to previously published criteria [5], which are as follows: (1) memory complaint, (2) normal activities of daily living, (3) normal general cognitive function, (4) abnormal memory for age, and (5) no sign of dementia. All patients with MCI underwent medical and neuropsychological reevaluation at approximately 3-month intervals and were divided into 2 groups: MCI converters (MCI-C; n = 7) and MCI nonconverters (MCI-NC; n = 7). MCI-C were defined as patients who eventually developed AD within a mean follow-up of 40.0 ± 6.9 months (range: 28–49 months), and MCI-NC were defined as patients having a transient memory loss or remaining cognitively stable for at least 3 years of follow-up (42.4 ± 2.2 months; range: 40–45 months). Aged volunteers who were taking no centrally active medication and who had no cognitive impairment or cerebrovascular lesion on MRI images were recruited as aged normal controls. All aged normal controls were screened via their medical history and responses to the MMSE. Subjects with medical conditions such as multiple cerebral infarctions, normal-pressure hydrocephalus, subdural hematoma, brain tumor, epilepsy, major depression, Parkinson's disease and other neurodegenerative diseases were excluded. In addition, asymptomatic cerebral infarction was not detected on T_2-weighted MRI images in the aged normal controls. The demographic data for all patients and aged normal controls are shown in table 1. The protocol of this study was approved by the Committee on Clinical Investigation at the Tohoku University School of Medicine, and by the Advisory Committee on Radioactive Substances at Tohoku University. Written informed consent was obtained from all patients and controls after complete description of the study. The clinical study was performed in accordance with the Declaration of Helsinki.

Radiosynthesis

BF-227 and its N-desmethylated derivative, a precursor to [^{11}C]BF-227, were synthesized by Tanabe R&D Service Co. (Osaka, Japan). [^{11}C]BF-227 was synthesized from the precursor by N-methylation in dimethyl sulfoxide, using [^{11}C]methyl triflate [10]. After quenching the reaction with 5% acetic acid in ethanol, [^{11}C]BF-227 was separated from the crude mixture by semipreparative, reversed-phase high-performance liquid chromatography and isolated from the collected fraction by solid-phase extraction. Purified [^{11}C]BF-227 was solubilized in isotonic saline containing 1% polysorbate 80 and 5% ascorbic acid. The saline solution was filter sterilized with a 0.22-μm Millipore filter (Millipore Co., Bedford, Mass., USA) for clinical use. At the end of synthesis, the radiochemical yields were greater than 50%, based on [^{11}C]methyl triflate, and the specific radioactivity ranged from 119 to 138 GBq/μmol. Radiochemical purities were greater than 95%.

Scanning Protocol

The [^{11}C]BF-227 PET study was performed using a SET-2400W PET scanner (Shimadzu, Kyoto, Japan). After intravenous injections of 211–366 MBq [^{11}C]BF-227, dynamic PET images were obtained for 60 min (23 sequential scans; 5 scans × 30 s, 5 scans × 60 s, 5 scans × 150 s, and 8 scans × 300 s) with closed eyes. All aged normal controls and patients underwent MRI using a 1.5-tesla MRI scanner (GE Signa Hispeed; GE Healthcare, Milwaukee, Wisc., USA). A 3-D volumetric acquisition of a T_1-weighted gradient echo sequence produced a gapless series of thin axial sections, using a vascular time-of-flight spoiled gradient echo sequence

Table 1. Demographic information on all the subjects

	Aged normal	MCI-NC	MCI-C	AD1	AD2	All AD
Number	12	7	7	10	9	19
Age, years	67.3 ± 2.7 (64–71)	77.6 ± 3.1* (74–82)	79.4 ± 4.2* (75–85)	72.9 ± 5.4 (65–85)	72.6 ± 7.3 (61–82)	72.7 ± 6.2 (61–85)
Gender (F/M), n	6/6	5/2	3/4	2/8	4/5	6/13
MMSE score	29.9 ± 0.3 (29–30)	26.3 ± 1.1 (25–28)	24.6 ± 3.4 (23–29)	22.7 ± 1.4* (21–25)	17.2 ± 2.9*,# (12–20)	20.1 ± 3.6 (12–25)
Years of education	13.2 ± 0.94	12.3 ± 0.48	11.9 ± 0.55	10.9 ± 0.72	10.3 ± 0.65	10.5 ± 0.42
GDS score	4.01 ± 0.44	4.32 ± 0.34	4.79 ± 0.31	4.23 ± 0.35	4.18 ± 0.46	4.20 ± 0.28

Values denote means ± SD with ranges in parentheses unless stated otherwise. Kruskal-Wallis test followed by Dunn's multiple comparison test. GDS = Geriatric Depression Scale. * $p < 0.05$ versus aged normal, # $p < 0.05$ versus MCI-NC.

(echo time/repetition time: 2.4/50 ms; flip angle: 45°; acquisition matrix: 256 × 256; 1 excitation; field of view: 22 cm; slice thickness: 2.0 mm).

Image Analysis

Standardized uptake value (SUV) images of [^{11}C]BF-227 were obtained by normalizing tissue concentration to injected dose and body weight. Average summations of SUV images were created from frames (20–40 min after injection) of dynamic PET images. Individual MR images were anatomically correlated with BF-227 PET images, using a statistical parametric mapping software (SPM5; Wellcome Department of Imaging Neuroscience, London, UK) [17]. ROI in the frontal cortex (Brodmann's areas, BA, 8, 9, 10, 44, 45, 46 and 47), lateral temporal cortex (BA 21, 22, 37 and 38), parietal cortex (BA 39 and 40), occipital cortex (BA 17), posterior cingulate cortex (BA 31) and cerebellar hemisphere were superimposed on MRI images, as described previously [10]. ROI information was then copied onto PET images, and regional SUV values at 20–40 min after injection were sampled using Dr. View/LINUX software (AJS, Tokyo, Japan). The cerebellum was used as the reference region. The regional-to-cerebellum SUV ratio (SUVR) was calculated and used as an index of BF-227 retention because the cerebellum is reported to be a region free of fibrillar amyloid plaques in the AD brain. Voxel-by-voxel comparisons between images from aged normal controls, patients with MCI and patients with AD were performed using SPM5 software. Spatial normalization was performed using an MR T_1 template of SPM5 to transfer PET images onto a standard stereotactic space. The normalized PET images were smoothed, using a 12 × 12 × 12 mm gaussian filter. The voxel count was normalized to the cerebellar ROI value. Images of the MCI-NC, MCI-C and AD groups, including patients with AD1 and AD2, were compared with those of the aged normal controls by means of a between-group analysis ($p < 0.05$ with false discovery rate correction; extent threshold: $k = 750$). For group analysis, a two-sample t test was used to detect differences among the groups.

In addition, a Z-score map of individual PET images was created for comparison between the mean and SD of the PET images of aged normal controls for each voxel. A software program named the Easy Z-Score Imaging System was used for this analysis [18]. Each PET SUV image was compared with the mean and SD of PET images of 15 aged normal controls (age: 58.9 ± 13.5 years; gender M/F: 10/5; MMSE score: 29.9 ± 0.2), using voxel-by-voxel Z-score analysis following voxel normalization to cerebellar ROI values according to the following formula: Z-score = (control mean – individual value)/control SD. Z-score maps were displayed by projection, with an averaged Z-score of 14 mm thickness to the surface rendering the anatomically standardized MRI template.

Neuropathological Staining

Postmortem brain tissue from an autopsy-confirmed AD case (87-year-old male) was obtained from the Tohoku University Hospital. Serial sections (6 μm thick) of paraffin-embedded blocks of temporal and frontal cortices were prepared in xylene and ethanol. Before staining, quenching of autofluorescence was performed by blanched sections in 0.25% potassium permanganate solution for 30 min. The sections were then treated with 0.1% potassium metabisulfite and 0.1% oxalic acid, followed by dipping briefly in water. The quenched tissue sections were immersed in 100 μmol/l of compound solution for 10 min and examined using a BX-51 fluorescence microscope (Olympus, Tokyo, Japan) equipped with a violet filter set (excitation: 380–420 nm; dichroic mirror: 430 nm; long-pass filter: 450 nm). Immunostaining was performed using monoclonal antibodies against Aβ (6F/3D; Dako, Glostrup, Denmark) at a dilution of 1:50. After pretreatment with formic acid for 5 min, the sections were placed in blocking solution for 30 min. After incubation with primary antibodies at 37°C for 60 min, the sections were processed by the avidin-biotin method using the Pathostain ABC-POD(M) kit (Wako) and chromogen DAB. The amyloid plaque morphology was classified into 2 types: (1) dense Aβ plaques including cored deposits with or without a ring of neuritic fibers, and (2) diffuse Aβ plaques including amorphous deposits. We randomly selected 20 areas (1.05 mm^2 per area) per section in the gray matter of the frontal and temporal cortices and counted the number of dense and diffuse Aβ plaques in each area. To estimate the capability of the compound to detect each kind of plaque, we examined the relationship between the number per unit area of positive staining using BF-227- and Aβ-specific antibody.

Statistical Analysis

Statistical comparisons of age among the 5 groups were performed using the Kruskal-Wallis test followed by Dunn's multiple comparison test. Statistical comparison of ROI results was performed via an analysis of variance followed by the Bonferroni method for multiple comparisons. Furthermore, effect size coefficients (Cohen's d) were calculated to evaluate group differences in PET measurements. The performance of diagnostic indices to

discriminate among groups was assessed using receiver operating characteristic (ROC) analysis. The area under the ROC curve (AUC) and SE were calculated and compared using GraphPad Prism software (GraphPad, San Diego, Calif., USA). Correlations between stainability of Aβ immunostaining and BF-227 staining were examined using the nonparametric Spearman rank correlation analysis. The paired t test was used to examine the difference in cored plaque density between the frontal and temporal cortices. Statistical significance for each analysis was defined as $p < 0.05$. These analyses were performed using GraphPad Prism software.

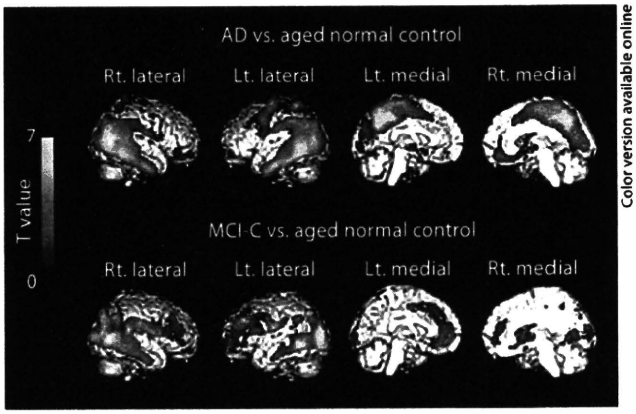

Fig. 1. Brain regions showing significantly higher uptake of [^{11}C] BF-227 in patients with AD (upper images) and MCI-C (lower images) compared with data from aged normal controls ($p < 0.05$, corrected for multiple comparisons). The red-to-yellow scale indicates the level of statistical significance of the differences in [^{11}C]BF-227 uptake (yellow: most significant difference).

Results

A statistically significant difference in age between aged normal controls and patients with MCI ($p < 0.05$) was observed. However, no statistically significant difference in age between MCI-C and MCI-NC as well as between aged normal controls and patients with AD was observed. Patients with AD showed a significantly lower MMSE score than aged normal controls. In addition, the AD2 group showed a significantly lower MMSE score than the MCI-NC group. However, no statistically significant difference in MMSE score was observed among other groups.

Voxel-based analysis of [^{11}C]BF-227 PET images demonstrated that MCI-C and patients with AD had significantly higher [^{11}C]BF-227 uptake in the neocortical region than aged normal controls (fig. 1; tables 2, 3). Bilateral temporoparietal BF-227 uptake was evident in both the AD and MCI-C groups although significant uptake in the posterior cingulate cortex and precuneus was observed only in the AD group. In the AD and MCI-C groups, the difference in the lateral frontal cortex was less evident compared with that in the lateral temporoparietal region. In contrast to the MCI-C group, the MCI-NC group showed no significant elevation of BF-227 uptake compared with the aged normal control group. Z-score maps of PET images were created by comparison with the normal control database (fig. 2). Most patients with AD showed a Z-score greater than 2 in the bilateral temporal and posterior cingulate cortices. In contrast, 10 out of the 12 aged normal controls (83%) showed no remarkable change in neocortical BF-227 uptake, except for 2 subjects (17%) showing modest changes in the lateral temporal and cingulate cortices. MCI-C tended to show higher neocortical Z-scores than MCI-NC (fig. 2b). Among the 7 MCI-C, 4 showed BF-227 uptake in the bilateral temporoparietal and frontal cortices, while the other 2 showed moderate abnormality in the temporal and frontal Z-scores. In MCI-C, changes in BF-227 uptake within the posterior cingulate cortex were relatively moderate compared with those in the lateral temporal cortex. One MCI-C showed limited change in BF-227 uptake within the temporal cortex and precuneus. In contrast to MCI-C, most MCI-NC showed no abnormal BF-227 uptake in the lateral temporal cortex, except for 1 who showed a slightly higher Z-score in the temporal cortex and an extremely high score in the posterior cingulate cortex. Another 3 MCI-NC also showed limited abnormality in the posterior cingulate cortex and precuneus but no abnormal Z-score in the lateral temporal cortex. No significant difference in BF-227 uptake was observed between the MCI-NC and MCI-C groups, MCI-NC and AD groups, and MCI-C and AD groups. Furthermore, no significant region showing reduction in BF-227 uptake in the MCI and AD groups compared with the aged normal controls was observed.

ROI analysis data were roughly consistent with voxel-based analysis data (fig. 3; table 4). The MCI-C group showed higher retention of [^{11}C]BF-227 in the frontal, temporal and parietal cortices than the aged normal control group. The AD1 group showed higher BF-227 retention in the frontal, temporal, parietal and occipital cortices than the aged normal control group. The AD2 group showed higher BF-227 retention in the temporal, parietal, occipital and posterior cingulate cortices than the aged normal control group, with the exception of the frontal cortex. Furthermore, significantly higher BF-227 uptake

Table 2. Talairach coordinates of within-cluster peak areas showing significantly higher BF-227 uptake in AD patients compared with aged normal group ($p < 0.05$, false discovery rate corrected)

k	T value	Talairach coordinates			Region
		x	y	z	
48,058	7.15 (5.38)	54	−46	−12	right inferior temporal gyrus
	6.79 (5.21)	50	−62	14	right middle temporal gyrus
	6.22 (4.92)	−52	−58	−2	left middle temporal gyrus
760	4.81 (4.09)	−24	4	−4	left putamen

Values in parentheses denote Z values.

Table 3. Talairach coordinates of within-cluster peak areas showing significantly higher BF-227 uptake in MCI-C compared with aged normal group ($p < 0.05$, false discovery rate corrected)

k	T value	Talairach coordinates			Region
		x	y	z	
14,893	6.19 (4.42)	46	−64	6	right middle temporal gyrus
	5.84 (4.27)	40	−74	14	right middle temporal gyrus
	5.52 (4.12)	52	−44	−8	right temporal lobe subgyrus
6,768	5.78 (4.24)	−36	32	34	left middle frontal gyrus
	4.78 (3.75)	−58	−16	24	left parietal lobe
	4.70 (3.71)	−24	50	0	left superior frontal gyrus
5,893	5.77 (4.24)	−38	−80	10	left middle occipital gyrus
	5.52 (4.12)	−42	−60	−4	left middle temporal gyrus
	5.27 (4.00)	−22	−92	−4	left cuneus

Values in parentheses denote Z values.

was found in the frontal and temporal cortices of the MCI-C group as well as in the temporal and parietal cortices of the AD group compared with the MCI-NC group. Compared with the AD group, Cohen's d was higher in the temporal (2.93) and parietal (2.25) cortices than in the frontal (1.69) and posterior cingulate (1.51) cortices for the aged normal control group. When comparing the MCI-C and MCI-NC groups, the highest Cohen's d was observed in the temporal (1.70) and parietal (1.76) cortices, followed by the frontal (1.62), posterior cingulate (0.85) and occipital (0.37) cortices, indicating that the difference in SUVR is the largest in the temporoparietal cortex when comparing the MCI-C and MCI-NC groups. Furthermore, ROC analysis demonstrated higher AUC values with the temporal SUVR (AUC = 0.987; SE = 0.016) than with the frontal SUVR (AUC = 0.915; SE = 0.052) for the discrimination between the AD and aged normal control groups as well as between the MCI-C and MCI-NC groups (fig. 4). Using the temporal BF-227 SUVR of 1.10 (1.5 SD above control mean) as the cutoff, a sensitivity of 95% and specificity of 92% in the discrimination between AD and aged normal groups, and a sensitivity of 100% and specificity of 57% in the discrimination between MCI-C and MCI-NC was achieved.

To explain why BF-227 preferentially accumulates in the temporal cortex as opposed to the frontal cortex of the AD brain, we examined the binding characteristics of BF-227 to Aβ deposits, using postmortem AD brain samples. BF-227 showed good stainability for dense-type plaques in the frontal and temporal cortices. Diffuse plaques in the frontal cortex tended to be larger than those in the temporal cortex. However, the stainability for diffuse-type plaques in the frontal cortex was relatively weaker than that in the temporal cortex (fig. 5). The mean number of Aβ plaques positively stained with BF-227 was significantly higher in the temporal cortex than in the fron-

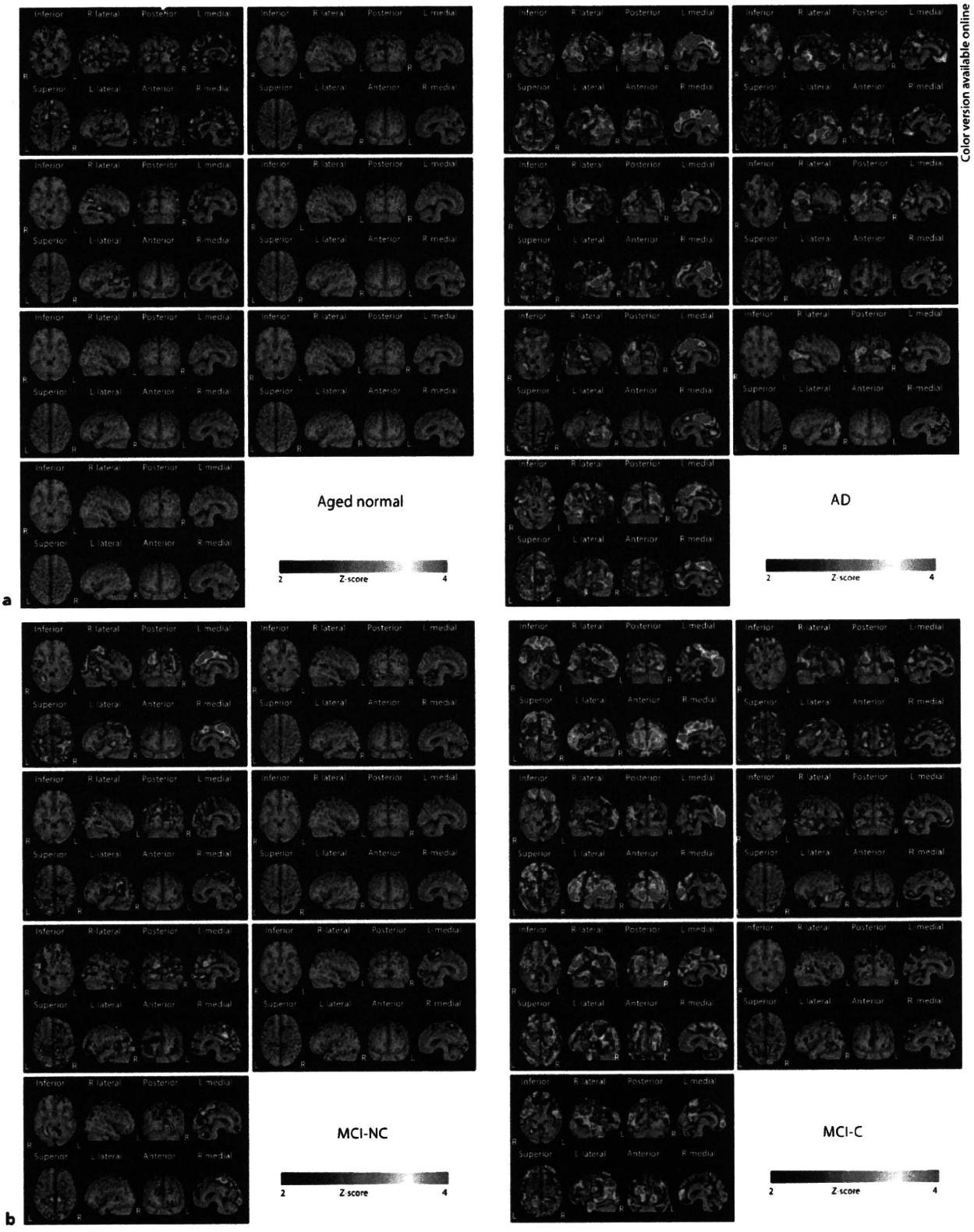
Color version available online
Aged normal
AD
MCI-NC
MCI-C
Z-score
2
4
a
b

Table 4. Average SUVR between 20 and 40 min after injection

	SUVR					Cohen's d	
	aged normal	MCI-NC	MCI-C	AD1	AD2	MCI-NC and MCI-C	aged normal and all AD
Frontal	0.98 ± 0.05	0.98 ± 0.06	1.11 ± 0.10*, #	1.08 ± 0.08*	1.06 ± 0.05	1.62	1.69
Temporal	1.02 ± 0.04	1.06 ± 0.07	1.18 ± 0.07*, #	1.18 ± 0.07*, #	1.18 ± 0.06*, #	1.7	2.93
Parietal	1.06 ± 0.04	1.08 ± 0.05	1.17 ± 0.05*	1.18 ± 0.06*, #	1.19 ± 0.09*	1.76	2.25
Occipital	1.05 ± 0.04	1.09 ± 0.06	1.11 ± 0.06	1.13 ± 0.07*	1.13 ± 0.05*	0.37	1.51
Posterior cingulate	1.11 ± 0.07	1.12 ± 0.07	1.19 ± 0.10	1.20 ± 0.09	1.22 ± 0.05*	0.85	1.51

Values denote means ± SD. * $p < 0.05$ versus aged normal group; # $p < 0.05$ versus MCI-NC group.

tal cortex. In the temporal cortex, the number of positively stained Aβ plaques showed a significantly positive correlation with the number of dense- and diffuse-type plaques. However, in the frontal cortex, the number of positively stained Aβ plaques showed a significant correlation with only the number of dense-type plaques and not with the number of diffuse-type plaques (fig. 6).

Discussion

The identification of patients with a high risk of developing AD in the MCI stage is of great clinical value. However, it is difficult to predict the conversion from MCI to AD from a clinical and neuropsychological perspective. In comparison with MRI and CT, PET is relatively expensive and not accessible. Consequently, PET is not routinely used in the diagnosis of AD. However, PET imaging provides useful diagnostic information for predicting conversion from MCI to AD when MRI fails to provide sufficient information [15]. A recent Pittsburgh compound B (PiB) PET study demonstrated that in vivo detection of amyloid deposition provides useful prognostic information in MCI [19]. The present study using BF-227 PET showed similar predictive performance to previous PiB PET results although the signal-to-background ratio increase for BF-227 in patients with AD over controls was considerably lower than that for PiB. The lower signal-to-background ratio of BF-227 would be due to the lower detection sensitivity of BF-227 than that of PiB for diffuse plaques. However, BF-227 PET may have a better predictive value for progression from MCI to AD than PiB PET because the deposition of diffuse plaque is observed even during the normal aging process. A head-to-head comparison of BF-227 PET with PiB PET will clarify which tracer has more predictive power for conversion of MCI to AD.

Voxel-based analysis of PET images allows an objective and sensitive identification of regional change in uptake of the tracer. BF-227 is a PET tracer that binds to amyloid plaques in the brain [10]. Although BF-227 binds well to amyloid fibrils in vitro, the signal-to-background ratio for [^{11}C]BF-227 PET images was relatively lower than that for PiB PET, possibly due to the lower binding affinity of BF-227 to Aβ fibrils compared to PiB. This drawback can be overcome by voxel-based statistical comparison with a normal control database. In fact, the abnormal distribution of [^{11}C]BF-227 in MCI-C was more clearly demonstrated by Z-score mapping analysis than by unprocessed SUVR images. In addition, a portion of MCI-NC showed a high Z-score in the posterior neocortical areas, which may reflect early Aβ pathology in the brain. The pathological significance of these abnormalities will be elucidated after having followed up these patients.

A commonly observed feature in the Z-score maps of MCI-C and patients with AD was the change in bilateral temporal and temporooccipital cortices, which was also detected by between-group comparison with the aged

Fig. 2. a Voxel-by-voxel Z-score analysis of [^{11}C]BF-227 PET images for aged normal subjects (left) and patients with AD (right) with the mean and SD of PET images of 15 normal controls. The Z-score maps were displayed by the surface projection of the spatially normalized MR image. **b** Voxel-by-voxel Z-score analysis by comparison of [^{11}C]BF-227 PET images for MCI-NC (left) and MCI-C (right) with the mean and SD of PET images of 15 normal controls. The Z-score maps were displayed by the surface projection of the spatially normalized MR image.

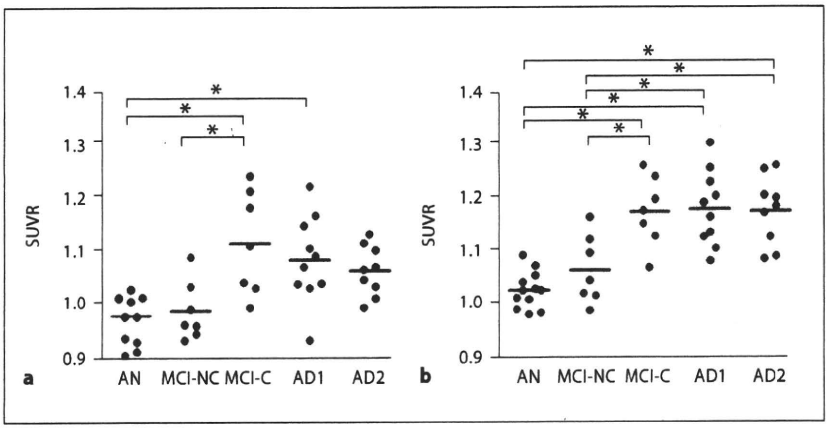

Fig. 3. Regional BF-227 SUVR in the frontal (**a**) and temporal (**b**) cortices. Horizontal bar: average SUVR in each group. * $p < 0.05$.

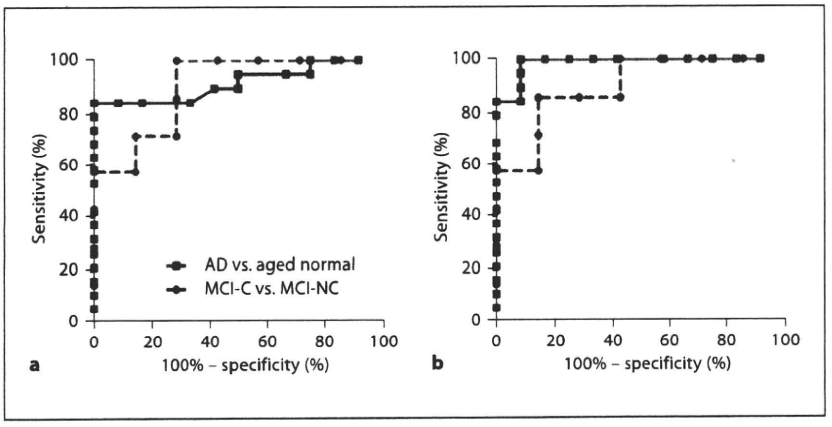

Fig. 4. ROC curves of regional BF-227 SUVR in the frontal (**a**) and temporal (**b**) cortices for differentiation between patients with AD and aged normal controls (solid line) and between MCI-C and MCI-NC (dashed line).

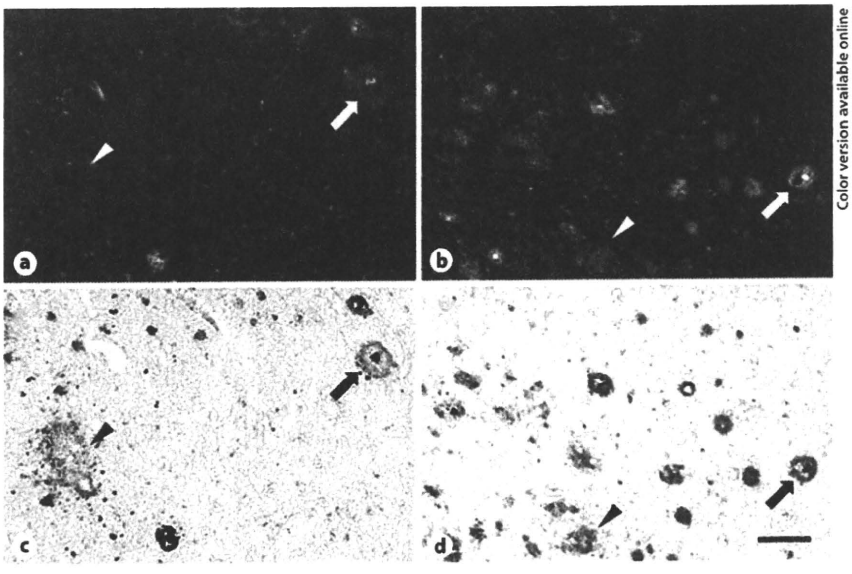

Fig. 5. Neuropathologic staining of AD frontal (**a**, **c**) and temporal (**b**, **d**) brain sections by BF-227. Cored plaques (arrows) are clearly stained with BF-227 (**a**, **b**). Cored-plaque staining with BF-227 correlates well with Aβ immunostaining in adjacent sections (**c**, **d**). Diffuse plaques (arrowheads) are faintly stained with BF-227 in the frontal brain section (**a**), but moderately stained in the temporal brain section (**b**). Scale bar = 100 μm.

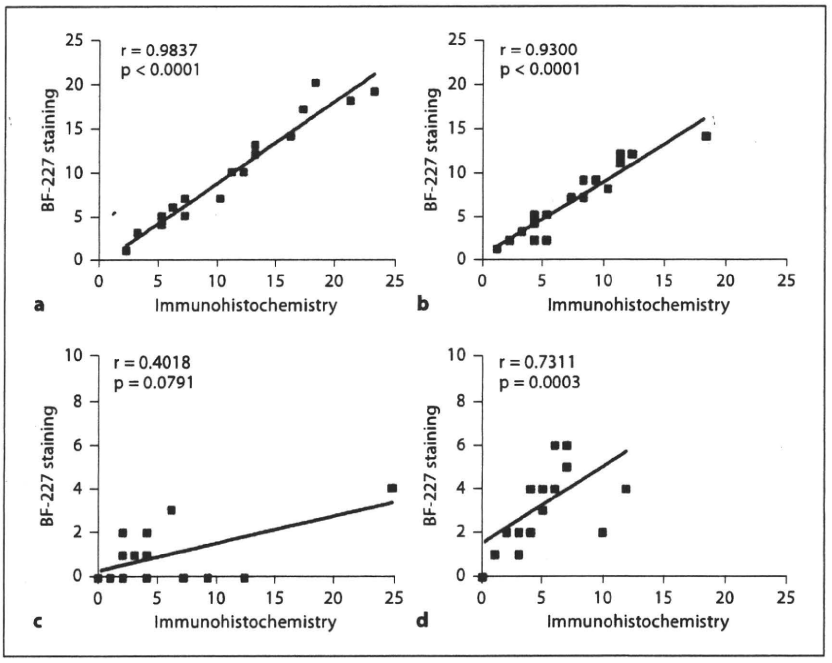

Fig. 6. Correlations between the numbers per unit area of amyloid plaques stained with Aβ-specific antibody and BF-227. The density of dense-type plaques showed a significant correlation with positive staining with BF-227 both in the frontal (**a**) and temporal (**b**) brain sections. However, the density of diffuse-type plaques was not correlated with BF-227 staining in the frontal cortex (**c**), and weakly correlated with BF-227 staining in the temporal cortex (**d**).

normal controls using the SPM software. The preferential [^{11}C]BF-227 retention in the posterior neocortical region corresponded with an area containing a high density of neuritic plaques [20]. This finding was confirmed by our analysis using postmortem AD brain samples. From these findings, the amount of dense plaque deposits in the posterior neocortical region, which could be measured by [^{11}C]BF-227 PET, is a reliable index of prognosis in patients with MCI. Interestingly, the Z-score mapping of BF-227 PET images further elucidated individual variation in the regional distribution of amyloid plaque deposition in patients with AD. There is great interest in determining the relationship between this heterogeneity and the clinical phenotype of patients with AD, which should be investigated in the future with data from a larger population. About 2/3 of patients with AD showed elevated BF-227 uptake in both anterior and posterior association areas, and the remaining 1/3 showed posterior-oriented BF-227 uptake. However, none of the patients with AD showed frontal-oriented BF-227 uptake. Although our analysis has been cross-sectional, these findings suggest that neuritic plaque deposition in AD starts at the posterior association areas and then spreads to other brain regions during AD progression.

The relatively lower [^{11}C]BF-227 retention in the frontal cortex of patients in the AD group may be a chance finding due to the small sample size. However, previous analysis of postmortem AD brain samples indicated that a majority of neocortical plaques start as fibrillar Aβ deposits and, in the late stages of AD, shift to nonfibrillar plaques [21]. Therefore, the relatively lower [^{11}C]BF-227 uptake in the AD group may be due to the transformation of fibrillar Aβ deposits to nonfibrillar Aβ deposits during AD progression. A longitudinal evaluation of [^{11}C]BF-227 uptake is necessary to examine whether the neocortical Aβ deposits reflected by BF-227 uptake change during the course of AD progression. In addition, the quantitative analysis of BF-227 binding to amyloid plaques should be performed in the future to eliminate the influence of regional cerebral hypoperfusion.

The definitive diagnosis of AD depends on postmortem examination because histological analysis of tissue samples is the only method for assessing AD pathology with certainty [7, 22]. Senile plaques were classified on the basis of the morphology of histopathological staining: diffuse plaques, primitive plaques, classical plaques and compacted plaques [23]. The diffuse plaques were abundant in healthy controls, whereas mature plaques such as primitive, classical and compact ones were typical in patients with AD. In our study, strong correlations between the number of mature plaques and BF-227 binding in the frontal and temporal cortices were observed. Further-

more, the temporal cortex exhibited a significant correlation between the number of diffuse-type plaques and BF-227 binding. However, the frontal cortex showed no such correlation. Generally, primitive, classical and compact plaques contain more amyloid fibrils than diffuse plaques. A previous electron microscopic examination has suggested that diffuse plaques in the frontal cortex contain a small amount of amyloid fibrils and do not easily transform to primitive plaques, while those in the temporal cortex contain more amyloid fibrils and tend to transform to primitive plaques [24]. Therefore, the binding ability of BF-227 to different types of diffuse plaques in the frontal and temporal cortices partly explains why BF-227 tends to accumulate in the temporal cortex of the AD brain. In addition, the density of dense-type plaques in the temporal cortex was higher than that in the frontal cortex in our analysis. This finding is in accordance with another comprehensive neuropathological examination that showed a higher density of amyloid plaques in the temporal cortex than in the frontal cortex [20, 25]. Thus, the lower density of primitive plaques in the frontal cortex may explain the relatively lower BF-227 uptake in the frontal cortex. Further analyses using more AD brain samples and radiolabeled BF-227 are required in the future because only one brain was examined in this study, and the concentration of BF-227 used to stain the postmortem tissue was not equivalent to the expected in vivo concentrations.

Previous PiB PET studies have shown the greatest tracer uptake in the precuneus and posterior cingulate cortex. However, our PET study demonstrated greater BF-227 uptake in the lateral temporal and parietal cortices of the AD brain samples than in the posterior cingulate cortex. A recent study demonstrated that the number of diffuse plaques in the posterior cingulate gyrus was greater than that in other neocortical areas. However, the number of neuritic plaques in the posterior cingulate cortex was not greater than that in other neocortical areas during AD progression [26]. Therefore, the modest posterior cingulate BF-227 uptake elevation in some patients with AD may be due to the lower binding affinity of BF-227 to diffuse plaques than that of PiB.

There are several limitations of this study. First, the sample size was small, primarily because of the limited follow-up period. Second, no repeat scans were performed to really assess changes in BF-227 uptake over time. Future studies should include longitudinal data from a larger sample. Third, the patients with MCI were older than the aged normal controls. Therefore, the higher neocortical uptake of [^{11}C]BF-227 in patients with MCI could be attributed to the effect of aging. However, no age-related change in BF-227 uptake was observed in the aged normal controls [10]. Furthermore, no significant elevation of [^{11}C]BF-227 uptake was observed in the MCI-NC group compared with that in the aged normal control group. Therefore, the higher [^{11}C]BF-227 uptake in the MCI-C group is not likely due to the effect of aging. We need to further address this issue by controlling for the age of normal controls and patients with MCI.

In summary, [^{11}C]BF-227 PET can detect the early Aβ load in the lateral temporal cortex of patients with MCI and AD. The amount of [^{11}C]BF-227 uptake in the temporal cortex was strongly related to prognosis in patients with MCI. BF-227 would be less subjective to amyloid pathology during the process of aging since this probe is believed to bind selectively to dense Aβ plaques. Thus, [^{11}C]BF-227 PET offers unique information concerning AD pathology that cannot be obtained by other PET tracers, which would be useful for the MCI population since it allows prediction of their risk for progression to AD in the near future.

Acknowledgments

This study was supported by the Health and Labor Sciences Research Grants for Translational Research from the Ministry of Health and the Grant-in-Aid for Scientific Research on Priority Areas – Integrative Brain Research from the Ministry of Education, Culture, Sports, Science, and Technology of Japan (20019006). We appreciate the technical assistance provided by Dr. S. Watanuki, Dr. Y. Ishikawa and M. Kato during the PET studies.

References

1 Glenner GG, Wong CW: Alzheimer's disease: initial report of the purification and characterization of a novel cerebrovascular amyloid protein. Biochem Biophys Res Commun 1984;120:885–890.

2 Masters CL, Multhaup G, Simms G, Pottgiesser J, Martins RN, Beyreuther K: Neuronal origin of a cerebral amyloid: neurofibrillary tangles of Alzheimer's disease contain the same protein as the amyloid of plaque core and blood vessels. EMBO J 1985;4:2757–2763.

3 Masters CL, Simms G, Weinman NA, Multhaup G, McDonald BL, Beyreuther K: Amyloid plaque core protein in Alzheimer disease and Down syndrome. Proc Natl Acad Sci USA 1985;82:4245–4249.

4 Hardy J, Selkoe DJ: The amyloid hypothesis of Alzheimer's disease: progress and problems on the road to therapeutics. Science 2002;297:353–356.

5 Petersen RC, Smith GE, Waring SC, Ivnik RJ, Tangalos EG, Kokmen E: Mild cognitive impairment: clinical characterization and outcome. Arch Neurol 1999;56:303–308.
6 Petersen RC: Mild cognitive impairment as a diagnostic entity. J Intern Med 2004;256: 183–194.
7 Ikonomovic MD, Klunk WE, Eric E, Abrahamson EE, Mathis CA, Price JC, Tsopelas ND, Lopresti BJ, Ziolko S, Bi WZ, Paljug WR, Debnath ML, Hope CE, Barbara A, Isanski BA, Hamilton RL, DeKosky ST: Post-mortem correlates of in vivo PiB-PET amyloid imaging in a typical case of Alzheimer's disease. Brain 2008;131:1630–1645.
8 Furumoto S, Okamura N, Iwata R, Yanai K, Arai H, Kudo Y: Recent advances in the development of amyloid imaging agents. Curr Top Med Chem 2007;7:1773–1789.
9 Klunk WE, Engler H, Nordberg A, Wang Y, Blomqvist G, Holt DP, Bergström M, Savitcheva I, Huang GF, Estrada S, Ausén B, Debnath ML, Barletta J, Price JC, Sandell J, Lopresti BJ, Wall A, Koivisto P, Antoni G, Mathis CA, Långström B: Imaging brain amyloid in Alzheimer's disease with Pittsburgh Compound-B. Ann Neurol 2004;55:306–319.
10 Kudo Y, Okamura N, Furumoto S, Tashiro M, Furukawa K, Maruyama M, Itoh M, Iwata R, Yanai K, Arai H: 2-(2-[2-dimethylaminothiazol-5-yl]ethenyl)-6-(2-[fluoro]ethoxy)benzoxazole: a novel PET agent for in vivo detection of dense amyloid plaques in Alzheimer's disease patients. J Nucl Med 2007;48:553–561.
11 Furukawa K, Okamura N, Tashiro M, Waragai M, Furumoto S, Iwata R, Yanai K, Kudo Y, Arai H: Amyloid PET in mild cognitive impairment and Alzheimer's disease with BF-227: comparison to FDG-PET. J Neurol 2010;257:721–727.
12 Verhoeff NP, Wilson AA, Takeshita S, Trop L, Hussey D, Singh K, Kung HF, Kung MP, Houle S: In vivo imaging of Alzheimer disease β-amyloid with [^{11}C]SB-13 PET. Am J Geriatr Psychiatry 2004;12:584–595.
13 Okamura N, Suemoto T, Shimadzu H, Suzuki M, Shiomitsu T, Akatsu H, Yamamoto T, Staufenbiel M, Yanai K, Arai H, Sasaki H, Kudo Y, Sawada T: Styrylbenzoxazole derivatives for in vivo imaging of amyloid plaques in the brain. J Neurosci 2004;24: 2535–2541.
14 Okamura N, Furumoto S, Funaki Y, Suemoto T, Kato M, Ishikawa Y, Ito S, Akatsu H, Yamamoto T, Sawada T, Arai H, Kudo Y, Yanai K: Binding and safety profile of novel benzoxazole derivative for in vivo imaging of amyloid deposits in Alzheimer's disease. Geriatr Gerontol Int 2007;7:393–400.
15 Waragai M, Okamura N, Furukawa K, Tashiro M, Furumoto S, Funaki Y, Kato M, Iwata R, Yanai K, Kudo Y, Arai H: Comparison study of amyloid PET and voxel-based morphometry analysis in mild cognitive impairment and Alzheimer's disease. J Neurol Sci 2009;285:100–108.
16 McKhann G, Drachman D, Folstein M, Katzman R, Price D, Stadlan EM: Clinical diagnosis of Alzheimer's disease: report of the NINCDS-ADRDA Work Group under the auspices of Department of Health and Human Services Task Force on Alzheimer's Disease. Neurology 1984;34:939–944.
17 Friston KJ, Holmes AP, Worsley KJ, Poline JP, Frith CD, Frackowiack RSJ: Statistical parametric maps in functional imaging: a general linear approach. Hum Brain Mapp 1995;2:189–210.
18 Matsuda H, Mizumura S, Nagao T, Ota T, Iizuka T, Nemoto K, Takemura N, Arai H, Homma A: Automated discrimination between very early Alzheimer disease and controls using an easy Z-score imaging system for multicenter brain perfusion single-photon emission tomography. AJNR Am J Neuroradiol 2007;28:731–736.
19 Okello A, Koivunen J, Edison P, Archer HA, Turkheimer FE, Någren K, Bullock R, Walker Z, Kennedy A, Fox NC, Rossor MN, Rinne JO, Brooks DJ: Conversion of amyloid positive and negative MCI to AD over 3 years: an ^{11}C-PiB PET study. Neurology 2009;73:754–760.
20 Arnold SE, Hyman BT, Flory J, Damasio AR, van Hoesen GW: The topographical and neuroanatomical distribution of neurofibrillary tangles and neuritic plaques in the cerebral cortex of patients with Alzheimer's disease. Cereb Cortex 1991;1:103–116.
21 Wegiel J, Bobinski M, Tarnawski M, Dziewiatkowski J, Popovitch E, Bobinski M, Lach B, Reisberg B, Miller D, de Santi S, de Leon MJ: Shift from fibrillar to nonfibrillar Aβ deposits in the neocortex of subjects with Alzheimer disease. J Alzheimers Dis 2001;3:49–57.
22 Braak H, Braak E: Neuropathological staging of Alzheimer-related changes. Acta Neuropathol 1991;82:239–259.
23 Dickson DW: The pathogenesis of senile plaques. J Neuropathol Exp Neurol 1997;56: 321–339.
24 Yamaguchi H, Nakazato Y, Shoji M, Takatama M, Hirai S: Ultrastructure of diffuse plaques in senile dementia of the Alzheimer type: comparison with primitive plaques. Acta Neuropathol 1991;82:13–20.
25 Cupidi C, Capobianco R, Goffredo D, Marcon G, Ghetti B, Bugiani O, Tagliavini F, Giaccone G: Neocortical variation of Aβ load in fully expressed, pure Alzheimer's disease. J Alzheimers Dis 2010;19:57–68.
26 Nelson PT, Abner EL, Scheff SW, Schmitt FA, Kryscio RJ, Jicha GA, Smith CD, Patel E, Markesbery WR: Alzheimer's-type neuropathology in the precuneus is not increased relative to other areas of neocortex across a range of cognitive impairment. Neurosci Lett 2009;450:336–339.

doi:10.1093/brain/awq091 Brain 2010: 133; 1772–1778 | 1772

BRAIN
A JOURNAL OF NEUROLOGY

In vivo visualization of α-synuclein deposition by carbon-11-labelled 2-[2-(2-dimethylaminothiazol-5-yl)ethenyl]-6-[2-(fluoro)ethoxy]benzoxazole positron emission tomography in multiple system atrophy

Akio Kikuchi,[1] Atsushi Takeda,[1] Nobuyuki Okamura,[2] Manabu Tashiro,[3] Takafumi Hasegawa,[1] Shozo Furumoto,[2,4] Michiko Kobayashi,[1] Naoto Sugeno,[1] Toru Baba,[1] Yasuo Miki,[5] Fumiaki Mori,[5] Koichi Wakabayashi,[5] Yoshihito Funaki,[4] Ren Iwata,[4] Shoki Takahashi,[6] Hiroshi Fukuda,[7] Hiroyuki Arai,[8] Yukitsuka Kudo,[9] Kazuhiko Yanai[2] and Yasuto Itoyama[1]

1 Department of Neurology, Graduate School of Medicine, Tohoku University, Sendai, 980-8574 Japan
2 Department of Pharmacology, Graduate School of Medicine, Tohoku University, Sendai, 980-8575 Japan
3 Division of Cyclotron Nuclear Medicine, Cyclotron and Radioisotope Centre, Tohoku University, Sendai, 980-8578 Japan
4 Division of Radiopharmaceutical Chemistry, Cyclotron and Radioisotope Centre, Tohoku University, Sendai, 980-8578 Japan
5 Department of Neuropathology, Institute of Brain Science, Hirosaki University Graduate School of Medicine, Hirosaki, 036-8562 Japan
6 Department of Diagnostic Radiology, Graduate School of Medicine, Tohoku University, Sendai, 980-8575 Japan
7 Department of Nuclear Medicine and Radiology, Institute of Development, Ageing and Cancer, Tohoku University, Sendai, 980-8575 Japan
8 Department of Geriatric and Respiratory Medicine, Institute of Development, Ageing and Cancer, Tohoku University, Sendai, 980-8575 Japan
9 Innovation of New Biomedical Engineering Centre, Tohoku University, Sendai, 980-8574 Japan

Correspondence to: Atsushi Takeda,
Department of Neurology,
Graduate School of Medicine,
Tohoku University,
1-1 Seiryo-machi,
Aoba-ku, Sendai, Miyagi,
980-8574, Japan
E-mail: atakeda@em.neurol.med.tohoku.ac.jp

The histopathological hallmark of multiple system atrophy is the appearance of intracellular inclusion bodies, named glial cytoplasmic inclusions, which are mainly composed of α-synuclein fibrils. *In vivo* visualization of α-synuclein deposition should be used for the diagnosis and assessment of therapy and severity of pathological progression in multiple system atrophy. Because 2-[2-(2-dimethylaminothiazol-5-yl)ethenyl]-6-[2-(fluoro)ethoxy] benzoxazole could stain α-synuclein-containing glial cytoplasmic inclusions in post-mortem brains, we compared the carbon-11-labelled 2-[2-(2-dimethylaminothiazol-5-yl)ethenyl]-6-[2-(fluoro)ethoxy] benzoxazole positron emission tomography findings of eight multiple system atrophy cases to those of age-matched normal controls. The positron emission tomography data demonstrated high distribution volumes in the subcortical white matter (uncorrected $P<0.001$), putamen and posterior cingulate cortex (uncorrected $P<0.005$), globus pallidus, primary motor cortex and anterior cingulate cortex (uncorrected $P<0.01$), and substantia nigra (uncorrected $P<0.05$) in multiple system atrophy cases compared to the normal controls. They were coincident with glial cytoplasmic inclusion-rich brain areas in

Received January 13, 2010. Revised March 15, 2010. Accepted March 17, 2010. Advance Access publication April 29, 2010

multiple system atrophy and thus, carbon-11-labelled 2-[2-(2-dimethylaminothiazol-5-yl)ethenyl]-6-[2-(fluoro)ethoxy] benzoxazole positron emission tomography is a promising surrogate marker for monitoring intracellular α-synuclein deposition in living brains.

Keywords: glial cytoplasmic inclusion; Lewy body; β-amyloid; Parkinson's disease; Pittsburgh compound B

Abbreviations: BF-227 = 2-[2-(2-dimethylaminothiazol-5-yl)ethenyl]-6-[2-(fluoro)ethoxy]benzoxazole; MSA = multiple system atrophy; PIB = Pittsburgh compound B

Introduction

Multiple system atrophy (MSA) is a sporadic, progressive neurodegenerative disease characterized by variable severity of parkinsonism, cerebellar ataxia, autonomic failure and pyramidal signs. Although MSA was originally described as three separate diseases [olivopontocerebellar atrophy (Dejerine and Thomas, 1900), striatonigral degeneration (van der Eecken *et al.*, 1960) and Shy–Drager syndrome (Shy and Drager, 1960)], they are currently classified into a single disease that consists of MSA with predominant parkinsonism and MSA with predominant cerebellar ataxia (Gilman *et al.*, 1999). The histopathological hallmark of MSA, glial cytoplasmic inclusions, comprises mainly insoluble fibrils of phosphorylated α-synuclein (Wakabayashi *et al.*, 1998). Thus, it is suggested that the MSA is in the family of α-synucleinopathies (Marti *et al.*, 2003) including Parkinson's disease and dementia with Lewy bodies, which are characterized by the presence of Lewy bodies, representing other brain inclusions composed of α-synuclein.

Previous neuropathological studies indicated that the appearance of glial cytoplasmic inclusions preceded the clinical onset of MSA (Fujishiro *et al.*, 2008) and the amount of α-synuclein deposition correlated with the disease progression (Wakabayashi and Takahashi, 2006). Therefore, it is plausible that the formation of α-synuclein deposits plays a key role in neurodegeneration, and that compounds that inhibit this process may be therapeutically useful for MSA and other α-synucleinopathies. In fact some compounds, including antioxidants (Ono and Yamada, 2006) and non-steroidal anti-inflammatory drugs (Hirohata *et al.*, 2008), were reported to have potent anti-fibrillogenic and fibril-destabilizing effects on aggregated α-synucleins, and received much attention as possible new therapeutic agents (Ono and Yamada, 2006; Hirohata *et al.*, 2008). Detection of α-synuclein deposition *in vivo* could theoretically allow early diagnosis even at the presymptomatic stage, as well as assess disease progression and possible therapeutic effects in the living brain of patients with MSA.

Although Pittsburgh compound B (PIB) and other compounds were reported to be useful in detecting senile plaques *in vivo*, to our knowledge, there were no imaging probes currently available for *in vivo* detection of α-synuclein deposition. Recently, 2-[2-(2-dimethylaminothiazol-5-yl)ethenyl]-6-[2-(fluoro)ethoxy] benzoxazole (BF-227), known as a positron emission tomography (PET) probe for *in vivo* detection of dense β-amyloid deposits in humans (Kudo *et al.*, 2007), was reported to bind with synthetic α-synuclein aggregates as well as β-amyloid fibrils *in vitro* (Fodero-Tavoletti *et al.*, 2009). In the present study, we demonstrated that BF-227 could stain α-synuclein-containing glial cytoplasmic inclusions in post-mortem tissues and moreover, that a PET study with carbon-11-labelled BF-227 ([11C]-BF-227) could detect α-synuclein deposits in the living brains of patients with MSA.

Materials and methods

Neuropathological staining

Brain specimens

The subjects of the first part of the study were nine autopsy cases, including three with Parkinson's disease, three with dementia with Lewy bodies and three with MSA. The above diagnoses were confirmed both clinically and histopathologically. Brain tissues taken from the temporal cortex and substantia nigra of patients with Parkinson's disease and dementia with Lewy bodies, and pontine base of patients with MSA, were fixed in 20% buffered formalin for 72 h at 4°C, and vibratome sections (50 μm thick) were prepared.

Fluorescence and immunohistochemical analysis

BF-227 was dissolved in 50% ethanol containing 5% polysorbate (Tween 80; Wako, Osaka, Japan). The sections were slide mounted, incubated in 100 μM BF-227 for 30 min, dipped three times in phosphate buffer, and coverslipped with non-fluorescent mounting medium (Vectashield, Vector Laboratories, Burlingame, CA, USA). Fluorescence images were visualized using an Olympus Provis fluorescence microscope (Olympus, Tokyo, Japan) at wavelength 400 nm. After photographing fluorescent structures, BF-227-labelled sections were immunostained with primary antibodies against phosphorylated α-synuclein (#64; Wako). For phosphorylated α-synuclein immunohistochemistry, the sections were pre-treated with 99% formic acid for 5 min, then incubated overnight at 4°C with each primary antibody followed by incubation with the biotinylated secondary antibodies and the avidin–biotin–peroxidase complex (Vectastain ABC kit, Vector Laboratories). Diaminobenzidine was used as the chromogen.

PET study

Subjects

Eight patients with probable MSA and eight age-matched normal subjects were studied to examine the distribution of [11C]-BF-227 in the brain. All probable MSA patients were diagnosed on the second consensus criteria for probable MSA (Gilman *et al.*, 2008). Table 1 summarizes the clinical features of these patients. There were no significant differences in age, disease duration and unified MSA rating scale score between the MSA with predominant parkinsonism

Table 1 Subject profile

	Normal controls	MSA		
		Total	MSA-P	MSA-C
n	8	8	4	4
Gender (F/M)	4/4	4/4	1/3	3/1
Age (years)	64.3 ± 5.90	57.4 ± 10.1	60.5 ± 11.1	54.3 ± 9.50
Duration (years)		1.50 ± 0.54	1.75 ± 0.50	1.25 ± 0.50
UMSARS score		36.1 ± 8.87	41.5 ± 9.39	30.8 ± 4.27

Data are mean ± SD.
MSA-P = MSA with predominant parkinsonism; MSA-C = MSA with predominant cerebellar ataxia; UMSARS = unified MSA rating scale.

subgroup and the MSA with predominant cerebellar ataxia subgroup. The normal control group comprised volunteers without impairment of cognitive and motor functions who had no cerebrovascular lesions on magnetic resonance imaging. The study protocol was approved by the Ethical Committee of Tohoku University Graduate School of Medicine, and a written informed consent was obtained from each subject after being given a complete description of the study.

Radiosynthesis of [^{11}C]-BF-227

BF-227 and its N-desmethylated derivative (a precursor of [^{11}C]-BF-227) were custom-synthesized by Tanabe R&D Service Co. (Tokyo) (Kudo *et al.*, 2007). [^{11}C]-BF-227 was synthesized from the precursor by N-methylation in dimethyl sulphoxide using [^{11}C]-methyl triflate (Jewett, 1992; Iwata *et al.*, 2001). After quenching the reaction with 5% acetic acid in ethanol, [^{11}C]-BF-227 was separated from the crude mixture by semi-preparative reversed-phase high-performance liquid chromatography and then isolated from the collected fraction by solid-phase extraction. The purified [^{11}C]-BF-227 was solubilized in isotonic saline containing 1% polysobate-80 and 5% ascorbic acid. The saline solution was filter sterilized with a 0.22 mm Millipore® filter for clinical use. The radiochemical yields were >50% based on [^{11}C]-methyl triflate, and the specific radioactivities were 119–138 GBq/mmol at the end of synthesis. The radiochemical purities were >95%.

PET procedure

The [^{11}C]-BF-227 PET study was performed using a SET-2400W PET scanner (Shimadzu Inc., Japan) under resting condition with eyes closed in a dark room. Following a 68Ge/Ga transmission scan of 300–400 s duration, an emission scan was started soon after intravenous injection of 3.7–8.3 mCi of [^{11}C]-BF-227. A dynamic series of PET scans were acquired over 60 min with 23 frames. Emission data were corrected for attenuation, dead time and radioactive decay. Standardized uptake value images were obtained by normalizing tissue concentration by the injected dose and body mass. Arterial blood samples (1.5 ml) from the radial or brachial artery were collected from each subject at 10 s intervals for the first 2 min, and subsequently at intervals increasing progressively from 1 to 10 min until 60 min after the injection of [^{11}C]-BF-227 except for one subject, from whom arterialized venous blood samples (1.5 ml) from a hand vein heated in a far-infrared mat were collected at the same time intervals. The plasma obtained by centrifugation at 3000*g* for 3 min was weighed and the radioactivity was measured with a well-type scintillation counter. Additional arterial blood samples were obtained at four time points during the study (5, 15, 30 and 60 min) for the determination of radiolabelled metabolites in plasma using high-performance liquid chromatography. These data yielded values of the unchanged fraction of parent radiotracer throughout the time frame of the study. A multi-exponential equation was used to describe this curve and to estimate the parent fraction at each measured plasma curve time point.

PET image analysis

To measure α-synuclein deposition densities in the brain, the distribution volume, the ratio of [^{11}C]-BF-227 concentration in tissue to that in plasma at equilibrium, was calculated by Logan's graphical analysis (Logan, 2000), since BF-227 reversibly binds to α-synuclein depositions (Tashiro *et al.*, 2009). Region of interest analysis was performed to evaluate the regional distribution of [^{11}C]-BF-227. Circular regions of interest were placed on individual axial PET images in the frontal cortex, primary motor cortex, parietal cortex, medial temporal cortex, lateral temporal cortex, occipital cortex, anterior cingulate cortex, posterior cingulate cortex, subcortical white matter, caudate nucleus, putamen, globus pallidus, thalamus, substantia nigra, midbrain tegmentum, pons and cerebellar cortex, referring to the individual magnetic resonance images.

Statistical analysis

Data were expressed as mean ± SD. Differences in distribution volume between normal control and MSA groups were evaluated by one-way analysis of variance followed by Bonferroni's multiple comparison test (GraphPad Prism Software).

Results

Neuropathological staining

In the post-mortem brains with Parkinson's disease, double-labelling immunostaining with BF-227 fluorostaining and anti-phosphorylated α-synuclein antibody demonstrated co-localization of the proteins in Lewy bodies in the substantia nigra (Fig. 1A and B). Strong BF-227 staining was observed in the central core (Fig. 1A). BF-227 was also detected in the cortical Lewy bodies in dementia with Lewy bodies (Fig. 1C and D). In MSA, double-labelling experiments using BF-227 and anti-phosphorylated α-synuclein antibody demonstrated BF-227 fluorescent signal in the most of glial cytoplasmic inclusions in the pontine base (Fig. 1E and F).

PET study

Tissue time activity curves of [^{11}C]-BF-227 in the brain indicated more gradual clearance from the brain in patients with MSA compared with normal subjects following initial rapid uptake of radioactivity (Fig. 2A). Relatively high concentrations of [^{11}C]-BF-227 radioactivity were observed in the subcortical white matter and lenticular nucleus in MSA, in which relatively intense α-synuclein deposits were found in the post-mortem brain (Fig. 2B). [^{11}C]-BF-227 exhibited linear regression curves on Logan plot analysis in all brain regions examined. Since the slopes of the regression lines represent the distribution volume of the tracer, these findings indicated a higher distribution volume of [^{11}C]-BF-227 in MSA than in normal controls (Fig. 2C). The regional distribution volume values were high in the subcortical white matter (uncorrected $P < 0.001$), putamen and posterior cingulate cortex

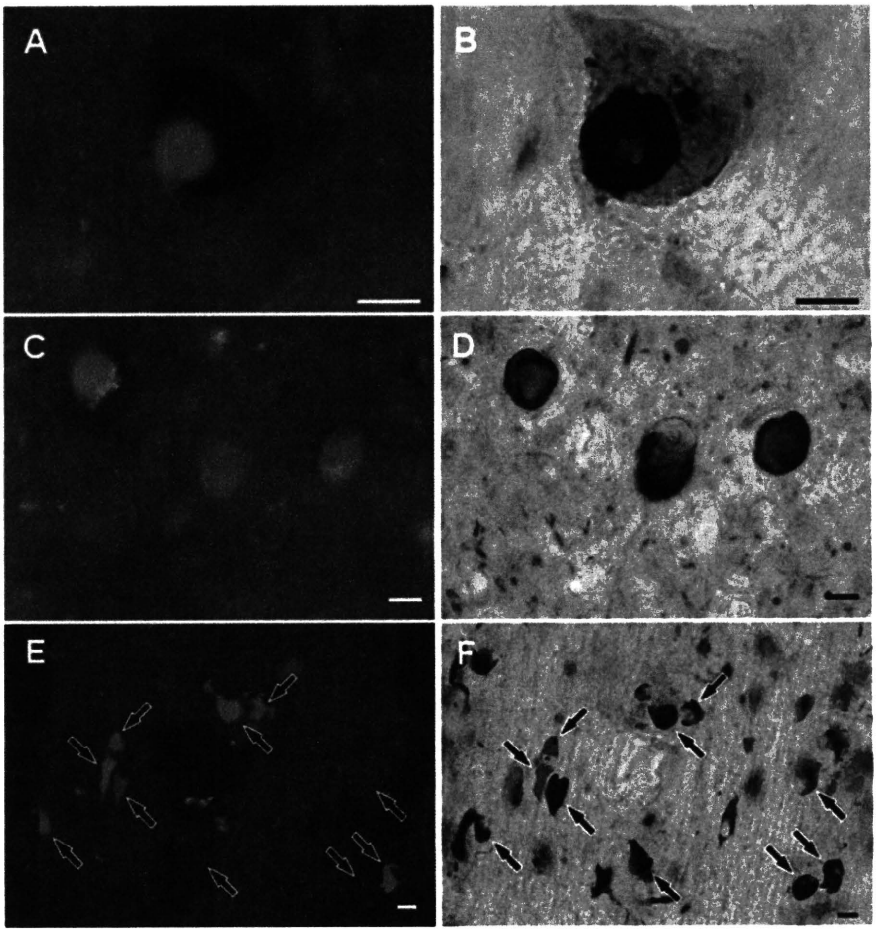

Figure 1 Neuropathological findings of BF-227 fluorostaining and anti-phosphorylated α-synuclein antibody immunostaining. BF-227 fluorostaining (**A** and **C**) and anti-phosphorylated α-synuclein antibody immunostaining (**B** and **D**) showed colocalization of these proteins in brainstem-type Lewy bodies in the substantia nigra of patients with Parkinson's disease (**A** and **B**) and in cortical Lewy bodies in the temporal lobe of patients dementia with Lewy bodies (**C** and **D**). Similarly, BF-227 fluorostaining (**E**) and anti-phosphorylated α-synuclein antibody immunostaining (**F**) were codetected in glial cytoplasmic inclusions in the pontine base of a patient with MSA. BF-227 histofluorescence was observed in the most of glial cytoplasmic inclusions (arrows). Bars = 10 μm.

(uncorrected $P<0.005$), globus pallidus, primary motor cortex and anterior cingulate cortex (uncorrected $P<0.01$) and substantia nigra (uncorrected $P<0.05$) in patients with MSA compared to the normal controls (Table 2 and Fig. 2D). It is noteworthy that the distribution volume of [^{11}C]-BF-227 was significantly high in the subcortical white matter even if Bonferroni's multiple comparison test was applied. On the other hand, no obvious differences were found in either the distribution or degree of binding between the MSA with predominant parkinsonism and MSA with predominant cerebellar ataxia subgroups.

Discussion

The BF-227 stained α-synuclein-containing Lewy bodies (Fig. 1A–D) and glial cytoplasmic inclusions (Fig. 1E and F) in formalin-fixed tissue sections as well as β-amyloid-containing senile plaques in paraffin-embedded tissue sections (Kudo *et al.*, 2007). These results were consistent with the previous findings showing BF-227 binding to synthetic α-synuclein fibrils with high affinity (K_d 9.63 nM) (Fodero-Tavoletti *et al.*, 2009), and to Lewy bodies in paraffin-embedded tissue sections (Fodero-Tavoletti *et al.*, 2009).

The anti-phosphorylated α-synuclein antibody immunostained the halo region more intensively compared with the central core in Lewy bodies in the substantia nigra of Parkinson's disease, while the BF-227 staining was intensely observed in the core of Lewy bodies (Fig. 1A and B). Because intense thioflavin S staining was also reported in the core of nigral Lewy bodies (Duda *et al.*, 2000), the core is thought to be rich in β-sheet structures. Similar to thioflavin S, the BF-227 staining is considered to recognize amyloid-like β-pleated sheets, and it was suggested to be the reason for the more intense BF-227 staining in the core of Lewy bodies. In addition, the high density of the core structure

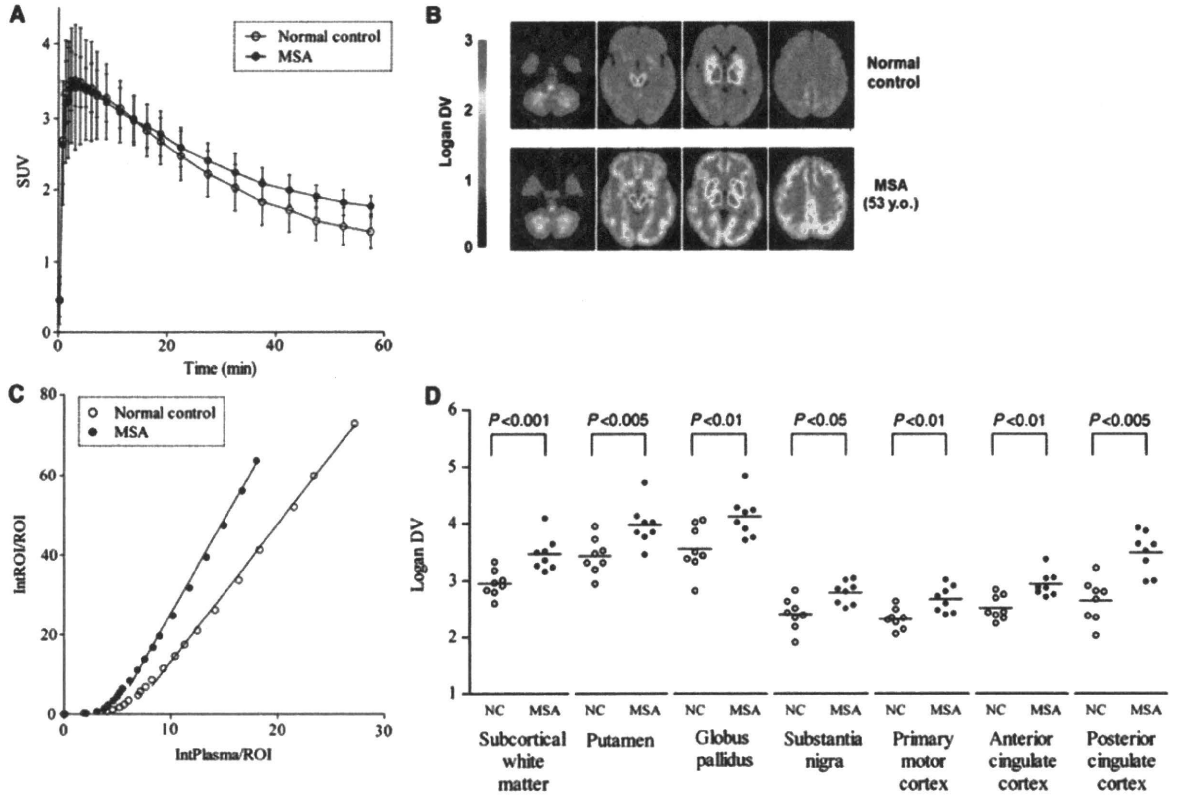

Figure 2 [^{11}C]-BF-227 PET findings in MSA. Time activity curves showed initial rapid uptake of radioactivity followed by gradual clearance in the putamen of both normal subjects and MSA cases. Data are mean ± SD of eight normal subjects and eight patients with MSA (**A**). In a representative patient with MSA with predominant cerebellar ataxia, the regional distribution volumes were mapped to the subcortical white matter and lentiform nucleus compared to normal control (**B**). Typical Logan plots for the putamen were presented in a representative patient with MSA with predominant cerebellar ataxia and a normal control. The slopes of the linear regression curves on Logan plot analysis represent the distribution volume of the tracer in the putamen (**C**). There were differences in the mean regional distribution volume values between patients with MSA and normal control in the subcortical white matter (uncorrected $P<0.001$), putamen and posterior cingulate cortex (uncorrected $P<0.005$), globus pallidus, primary motor cortex and anterior cingulate cortex (uncorrected $P<0.01$) and substantia nigra (uncorrected $P<0.05$). Data of individual subjects (symbols) and mean values (horizontal lines) (**D**). SUV = standardized uptake value; DV = distribution volume; ROI = region of interest.

may often prevent the penetration of antibodies into this region (Galloway *et al.*, 1992), since electron microscopic studies revealed that vesicular structures were tightly packed in the core of Lewy bodies (Takahashi and Wakabayashi, 2005). On the other hand, not all glial cytoplasmic inclusions stained by anti-phosphorylated α-synuclein antibody were always positive for BF-227 staining (Fig. 1E and F). In the process of oligodendroglial pathology, it was believed that α-synuclein deposits as amorphous state and then forms fibrillar structures (Gai *et al.*, 2003; Stefanova *et al.*, 2005). In fact, part of glial cytoplasmic inclusions were reported to be α-synuclein-negative (Sakamoto *et al.*, 2005) and therefore, it seems reasonable that some of glial cytoplasmic inclusions were not composed of β-sheet fibrils and were negative for BF-227 staining.

The regional distribution volume of [^{11}C]-BF-227 was the highest in the subcortical white matter, followed by the putamen, posterior cingulate cortex, anterior cingulate cortex, globus pallidus, primary motor cortex and substantia nigra, in which glial cytoplasmic inclusions were densely distributed (Papp and Lantos, 1994; Inoue *et al.*, 1997; Wakabayashi and Takahashi, 2006) and large increases of α-synuclein content were found (Tong *et al.*, 2010) in the post-mortem brains. Thus, it was suggested that the distributions of [^{11}C]-BF-227 could properly reflect those of the α-synuclein deposits *in vivo*. On the other hand, the regional distribution volume in other affected brain regions, such as the cerebellum and pons (Ozawa *et al.*, 2004; Wakabayashi and Takahashi, 2006), did not show higher values relative to the normal control group. The glial cytoplasmic inclusions in cerebellum were reported to decrease along with the disease progression and concomitant neuronal loss (Inoue *et al.*, 1997). Therefore, it is plausible that the accumulation levels of glial cytoplasmic inclusions are changing and do not always increase with the disease progression (Mochizuki *et al.*, 1992; Inoue *et al.*, 1997). Moreover, due to the remarkable cerebellar and pontine atrophy,

Table 2 Distribution volume of [^{11}C]BF-227

	Normal controls	MSA
Frontal cortex	2.28 ± 0.18	2.46 ± 0.22
Primary motor cortex	2.40 ± 0.28	2.79 ± 0.20¶
Parietal cortex	2.48 ± 0.26	2.63 ± 0.24
Medial temporal cortex	2.44 ± 0.21	2.82 ± 0.31
Lateral temporal cortex	2.42 ± 0.19	2.63 ± 0.23
Occipital cortex	2.43 ± 0.20	2.72 ± 0.27
Anterior cingulate cortex	2.32 ± 0.18	2.67 ± 0.23¶
Posterior cingulate cortex	2.52 ± 0.22	2.94 ± 0.22†
Subcortical white matter	2.65 ± 0.38	3.49 ± 0.36‡
Caudate nucleus	2.70 ± 0.21	3.05 ± 0.34
Putamen	2.95 ± 0.23	3.47 ± 0.30†
Globus pallidus	3.43 ± 0.31	3.97 ± 0.36¶
Thalamus	3.50 ± 0.28	4.03 ± 0.31
Substantia nigra	3.55 ± 0.41	4.12 ± 0.36*
Midbrain tegmentum	3.53 ± 0.54	3.45 ± 0.47
Pons	3.63 ± 0.54	3.88 ± 0.42
Cerebellar cortex	2.32 ± 0.22	2.16 ± 0.29

Data are mean ± SD.
*Uncorrected $P < 0.05$.
¶Uncorrected $P < 0.01$.
†Uncorrected $P < 0.005$.
‡Uncorrected $P < 0.001$.

the distribution volume in these regions might be underestimated. Correction for partial volume loss is therefore needed to improve the accuracy of quantification in the cerebellum and brainstem of MSA. BF-227 fluorescent signal was detected in β-amyloid plaques as well as glial cytoplasmic inclusions and Lewy bodies (Fig. 1A–F) in neuropathological staining (Kudo *et al.*, 2007). However, the differences in the distribution of [^{11}C]-BF-227 by PET could discriminate MSA from Alzheimer's disease, which showed high distribution of [^{11}C]-BF-227 in the temporoparietal–occipital region (Kudo *et al.*, 2007). In our preliminary studies, Parkinson's disease and dementia with Lewy bodies also showed quite different patterns of distribution volumes from those of MSA (data not shown). Therefore, MSA could be distinguished from other degenerative diseases such as Alzheimer's disease, Parkinson's disease and dementia with Lewy bodies by the [^{11}C]-BF-227 PET.

The affinity of BF-227 to α-synuclein fibrils (K_d 9.63 nM) was reported to be almost identical to that of PIB (K_d 10.07 nM) (Fodero-Tavoletti *et al.*, 2007, 2009). However, in the post-mortem human brain, the PIB binding was not colocalized with α-synuclein-positive Lewy bodies in two reports (Fodero-Tavoletti *et al.*, 2007; Ye *et al.*, 2008) although one report showed PIB binding to Lewy bodies in the substantia nigra of Parkinson's disease (Maetzler *et al.*, 2008). Therefore, there is controversy as to whether PIB binds to α-synuclein-containing Lewy bodies. Moreover, there have been no reports showing that PIB could detect α-synuclein deposits in α-synucleinopathies by PET (Fodero-Tavoletti *et al.*, 2007; Johansson *et al.*, 2008; Maetzler *et al.*, 2008). The hydroxy group in PIB (Mathis *et al.*, 2003) may prevent it from passing through the cell membranes and thereby detecting α-synuclein depositions in the cytoplasm, however, the BF-227 is more lipophilic than PIB (Mathis *et al.*, 2003), and may easily pass into the cytoplasm and bind to α-synuclein aggregates. As shown in the present study, BF-227 is a promising tracer to detect glial cytoplasmic inclusions. Further studies are warranted to verify whether Lewy bodies in other α-synucleinopathies as well as glial cytoplasmic inclusions can be detected by [^{11}C]-BF-227 PET.

In conclusion, the BF-227 could bind to α-synuclein-containing glial cytoplasmic inclusions (Fig. 1E and F) in the post-mortem brain, and the [^{11}C]-BF-227 PET demonstrated high signals in the glial cytoplasmic inclusion-rich brain regions including subcortical white matter, putamen, globus pallidus, primary motor cortex and anterior and posterior cingulate cortex (Table 2 and Fig. 2D). These results suggest that [^{11}C]-BF-227 PET is a suitable surrogate maker for monitoring α-synuclein deposits in living brains with MSA and could be a potential tool to monitor the effectiveness of neuroprotective therapy for α-synucleinopathies.

Funding

Grant for 'the Research Committee for Ataxic Diseases' of the Research on Measures for Intractable Diseases from the Ministry of Health, Labour and Welfare, Japan (partial).

References

Dejerine J, Thomas A. L'atrophie olivo-ponto-cérébelleuse. Nouvelle Iconographie Salpêtrière 1900; 13: 330–7.

Duda JE, Lee VM, Trojanowski JQ. Neuropathology of synuclein aggregates. J Neurosci Res 2000; 61: 121–7.

Fodero-Tavoletti MT, Mulligan RS, Okamura N, Furumoto S, Rowe CC, Kudo Y, et al. In vitro characterisation of BF227 binding to alpha-synuclein/Lewy bodies. Eur J Pharmacol 2009; 617: 54–8.

Fodero-Tavoletti MT, Smith DP, McLean CA, Adlard PA, Barnham KJ, Foster LE, et al. In vitro characterization of Pittsburgh compound-B binding to Lewy bodies. J Neurosci 2007; 27: 10365–71.

Fujishiro H, Ahn TB, Frigerio R, DelleDonne A, Josephs KA, Parisi JE, et al. Glial cytoplasmic inclusions in neurologically normal elderly: prodromal multiple system atrophy? Acta Neuropathol 2008; 116: 269–75.

Gai WP, Pountney DL, Power JH, Li QX, Culvenor JG, McLean CA, et al. alpha-Synuclein fibrils constitute the central core of oligodendroglial inclusion filaments in multiple system atrophy. Exp Neurol 2003; 181: 68–78.

Galloway PG, Mulvihill P, Perry G. Filaments of Lewy bodies contain insoluble cytoskeletal elements. Am J Pathol 1992; 140: 809–22.

Gilman S, Low PA, Quinn N, Albanese A, Ben-Shlomo Y, Fowler CJ, et al. Consensus statement on the diagnosis of multiple system atrophy. J Neurol Sci 1999; 163: 94–8.

Gilman S, Wenning GK, Low PA, Brooks DJ, Mathias CJ, Trojanowski JQ, et al. Second consensus statement on the diagnosis of multiple system atrophy. Neurology 2008; 71: 670–6.

Hirohata M, Ono K, Morinaga A, Yamada M. Non-steroidal anti-inflammatory drugs have potent anti-fibrillogenic and fibril-destabilizing effects for alpha-synuclein fibrils in vitro. Neuropharmacology 2008; 54: 620–7.

Inoue M, Yagishita S, Ryo M, Hasegawa K, Amano N, Matsushita M. The distribution and dynamic density of oligodendroglial cytoplasmic inclusions (GCIs) in multiple system atrophy: a correlation between the density of GCIs and the degree of involvement of striatonigral and olivopontocerebellar systems. Acta Neuropathol 1997; 93: 585–91.